

Docking of Lytic Granules at the Immunological Synapse in Human CTL Requires Vti1b-Dependent Pairing with CD3 Endosomes

Bin Qu,^{*1} Varsha Pattu,^{†1} Christian Junker,^{*} Eva C. Schwarz,^{*} Shruthi S. Bhat,^{*} Carsten Kummerow,^{*} Misty Marshall,[†] Ulf Matti,[†] Frank Neumann,[‡] Michael Pfreundschuh,[‡] Ute Becherer,[†] Heiko Rieger,[§] Jens Rettig,[†] and Markus Hoth^{*}

Lytic granule (LG)-mediated apoptosis is the main mechanism by which CTL kill virus-infected and tumorigenic target cells. CTL form a tight junction with the target cells, which is called the immunological synapse (IS). To avoid unwanted killing of neighboring cells, exocytosis of lytic granules (LG) is tightly controlled and restricted to the IS. In this study, we show that in activated human primary CD8⁺ T cells, docking of LG at the IS requires tethering LG with CD3-containing endosomes (CD3-endo). Combining total internal reflection fluorescence microscopy and fast deconvolution microscopy (both in living cells) with confocal microscopy (in fixed cells), we found that LG and CD3-endo tether and are cotransported to the IS. Paired but not single LG are accumulated at the IS. The dwell time of LG at the IS is substantially enhanced by tethering with CD3-endo, resulting in a preferential release of paired LG over single LG. The SNARE protein Vti1b is required for tethering of LG and CD3-endo. Downregulation of Vti1b reduces tethering of LG with CD3-endo. This leads to an impaired accumulation and docking of LG at the IS and a reduction of target cell killing. Therefore, Vti1b-dependent tethering of LG and CD3-endo determines accumulation, docking, and efficient lytic granule secretion at the IS. *The Journal of Immunology*, 2011, 186: 6894–6904.

Cytotoxic T lymphocytes are considered key players in the immune response to eliminate tumorigenic or virus-infected target cells (1–5). CTL cytotoxicity is mainly mediated by exocytosis of lytic granules (LG) and the Fas pathway (6). To kill cognate target cells efficiently, CTL and target cells form a close connection, called the immunological synapse (IS), upon TCR engagement by matching peptide–MHC complexes (4, 7, 8). Formation of the IS involves drastic morphological changes and cell polarization, which facilitates the stable physical contact between the two cells (4, 9) leading to CTL activation and target cell death (2). TCR are constitutively internalized and recycled back to the cell surface and are quickly

enriched at the IS after its formation (10–12). This is necessary to recruit effector molecules and initiate downstream signaling that leads to target cell death (13, 14).

LG, which contain perforin and granzymes (15), are transported, docked, and released at the IS and induce target cell apoptosis (2, 16, 17). The directed secretion of LG is Ca²⁺ dependent (18), and it is critical to ensure the selective killing of a cognate target cell. Upon target cell recognition, CTL undergo large-scale rearrangements of the cytoskeleton. In NK cells, actin polymerization is required for receptor clustering, granule polarization (19), and cytotoxic function (20). The convergence of LG to the microtubule organizing center (MTOC) depends on dynein (21), and myosin IIA is required for interaction of LG and F-actin as well as the subsequent release of LG (22). In mouse CTL, the MTOC has even been shown to deliver LG to the IS by touching the plasma membrane (23). There is currently substantial excitement in elucidating the molecular mechanisms of LG polarization to the secretory domain of the CTL–target contact zone (4, 24). Jenkins et al. (25) have shown that the strength of the TCR signal is exceptionally important for LG accumulation at the IS, and Beal et al. (26) unmasked the kinetics of a short and long path of LG to the synapse.

The importance of CTL for the immune response is highlighted by life-threatening diseases: dysfunction of LG release is associated with familial hemophagocytic lymphohistiocytosis (FHL) or acquired hemophagocytic lymphohistiocytosis (27–29). Among the known causes of FHL are mutations in perforin (FHL2) (27), Munc13-4 (FHL3) (30), syntaxin11 (FHL4) (31), and Munc18-2 (FHL5) (32). In addition, Vti1b and Vamp8 are important for the killing capacity of CTL (33).

These diseases illustrate the importance of directed transport regulated by soluble *N*-ethylmaleimide-sensitive factor attachment receptor (SNARE) and/or SNARE-related proteins in targeting LG to the IS. SNARE proteins play a central role in

^{*}Department of Biophysics, Saarland University, 66421 Homburg, Germany;

[†]Department of Physiology, Saarland University, 66421 Homburg, Germany;

[‡]Department of Internal Medicine I, Saarland University, 66421 Homburg, Germany; and

[§]Department of Theoretical Physics, Saarland University, 66041 Saarbrücken, Germany

¹B.Q. and V.P. contributed equally to this work.

Received for publication October 20, 2010. Accepted for publication April 11, 2011.

This work was supported by the Deutsche Forschungsgemeinschaft (Graduate Program on Calcium Signalling and Cellular Nanodomains, Grants RE 1092/6-1 and SFB 894 to J.R. and M.H.), by the Deutsche Krebshilfe (to M.P.), and by a Homburger Forschungsförderung grant from the Medical Faculty, Saarland University, Homburg, Germany (to J.R., M.H., and E.C.S.).

Address correspondence and reprint requests to Prof. Markus Hoth or Prof. Jens Rettig, Institute of Biophysics, Saarland University, Building 58, 66421 Homburg, Germany (M.H.) or Institute of Physiology, Saarland University, Building 59, 66421 Homburg, Germany (J.R.). E-mail addresses: markus.hoth@uks.eu (M.H.) and jrettig@uks.eu (J.R.)

The online version of this article contains supplemental material.

Abbreviations used in this article: CD3-endo, CD3-containing endosomes; 4D, four-dimensional; FHL, familial hemophagocytic lymphohistiocytosis; LG, lytic granule; MTOC, microtubule organizing center; qRT-PCR, quantitative real-time PCR; SEA, staphylococcal enterotoxin A; siRNA, small interfering RNA; SNARE, soluble *N*-ethylmaleimide-sensitive factor attachment receptor; Stx11, syntaxin 11; TfR, transferrin receptors; TIRF, total internal reflection fluorescence.

Copyright © 2011 by The American Association of Immunologists, Inc. 0022-1767/11/\$16.00

budding, target selection, and fusion of intracellular compartments (34–36). It has been reported that SNARE proteins are also involved in focal and multidimensional pathways of cytokine release in T cells (37). The 36 mammalian SNAREs can be defined as either Q- (Qa, Qb, Qc or Qbc) or R-SNAREs, depending on which conservative residue the SNARE protein contributes at layer 0 within the four-helix bundle of SNARE complexes. SNARE proteins mediate membrane fusion in all trafficking steps of the secretory pathway. Prior to fusion, SNAREs on opposing membranes are able to form four helix bundles that lead to a tight connection of vesicular and target membranes (36).

We report that tethering (or pairing) of LG and CD3-containing endosomes (CD3-endo) is required for the enrichment, docking, and release of LG at the IS, which is needed for CTL-dependent target cell killing. In addition, we unmask that LG/CD3-endo tethering requires the Qb-SNARE protein Vti1b.

Materials and Methods

Abs and reagents

All chemicals not specifically mentioned were from Sigma (highest grade). The reagents used in our experiments include Alexa⁴⁸⁸-labeled anti-CD3 mAb (UCHT1; Biologend), Alexa⁶⁴⁷-labeled anti-CD3 mAb (UCHT1; Biologend), Alexa⁶⁴⁷-labeled anti-perforin mAb (dG9; Biologend), FITC-labeled anti-perforin mAb (dG9; ImmunoTools), Alexa⁵⁶⁸ goat anti-rabbit secondary Ab and Alexa⁵⁶⁸ goat anti-mouse secondary Ab (Invitrogen), rabbit polyclonal anti-Vti1b Ab (Synaptic Systems), anti-Vti1b mAb (BD Biosciences), Alexa⁴⁸⁸-labeled transferrin (Invitrogen), anti- γ -tubulin Ab (Sigma), and anti-GM130 Ab (BD Biosciences). For total internal reflection fluorescence (TIRF) microscopy, the Abs against human CD3 (BB11; Euroclone) and CD28 (BD Biosciences) were used for coating the coverslips.

Construction of cDNA

Perforin, Rab5, Rab7, and Rab11 were amplified from human cDNA. Perforin was ligated to mCherry at the C terminus and then purified. Rab5, Rab7, and Rab11 were ligated to mCherry at the N terminus and then purified. The mCherry construct was obtained as a gift from Roger Tsien (Howard Hughes Medical Institute, University of California, San Diego, La Jolla, CA). Perforin–mCherry overlapped with the perforin–Ab staining (Supplemental Fig. 3A), indicating that the mCherry fluorescence was contained in LG (38). The γ -tubulin–GFP construct was a kind gift from Alexey Khodjakov (Wadsworth Center).

Cell culture and nucleofection of CD8⁺ T cells

Research carried out for this study with human material has been approved by the local ethics committee. Human PBL were obtained from healthy donors as described previously (39). PBL were stimulated with staphylococcal enterotoxin A (SEA; 5 μ g/ml) at a density of 1×10^8 cells/ml at 37°C for 1 h and then resuspended at a density of 2×10^6 cells/ml in AIMV medium (Invitrogen) supplemented with 10% FCS and 100 U/ml recombinant human IL-2 (Biosource). After 5 d, SEA-specific CTL were positively isolated using a Dynal CD8 positive isolation kit (Invitrogen). Purified SEA-specific CTL were maintained in AIMV medium supplemented with 10% FCS and 100 U/ml recombinant human IL-2 (Invitrogen). The CTL were used for experiments 2–3 d after the positive isolation. To introduce constructs or small interfering RNA (siRNA) into CTL, CTL were nucleofected using Human T Cell Nucleofector Kit (Lonza) and Nucleofector II (Lonza).

Generation of CMV-derived epitope-specific CD8⁺ bulk CTL

PBMC obtained from a CMV⁺ donor were isolated by Ficol-Paque PLUS separation (GE Healthcare Bio-Sciences AB, Uppsala, Sweden), and the CD8⁺ T lymphocytes were magnetically enriched using CD8 MicroBeads according to the supplier's protocol (Miltenyi Biotec, Bergisch Gladbach, Germany). The nonamer peptide spanning the amino acid sequence of the pp65 Ag derived from the human CMV from aa 495 to aa 503 is in general known as an epitope inducing strong CTL immune responses in the context of HLA-A*0201. Peptide p495–503 was synthesized following the Fmoc/tBu strategy as described by others (40). Purity was >85% as assessed by HPLC and mass spectrometry. The peptide was dissolved in a mixture of water and DMSO. For in vitro priming, the CD8⁺ cells were suspended in serum-free X-Vivo medium (Lonza, Verviers, Belgium) supplemented with

2 mM L-glutamine (Life Technologies, Invitrogen, Karlsruhe, Germany) and 1% penicillin/streptomycin (Life Technologies) and pulsed with peptide p495–503 (2 μ M, 37°C, 1.5 h). Thereafter cells were washed, irradiated with 30 Gy, and resuspended in X-Vivo medium with 10% human AB serum and served as APC. The same number of CD8⁺ T cells were cocultured as prospective effector cells. At days 7 and 14, the CD8⁺ effector cells were restimulated using peptide-pulsed CD8⁺ APC under identical conditions. At day 14, specificity of the stimulated effector cells was assessed by IFN- γ segregation using an ELISPOT assay as described previously (41).

Establishment of epitope-specific CD8⁺ T cell clones

Responding T cells were isolated out of the bulk population by IFN- γ -based magnetic cell enrichment using a cytokine-secretion assay (Miltenyi Biotec) and cloned by limiting-dilution culture, following a protocol described by zum Büschenfelde et al. (42). Specifically reacting CD8⁺ clones were expanded by restimulation performed after 14 d under identical conditions. Cytotoxicity of CD8⁺ T cells from CTL clone KL-1/#35 against peptide-pulsed and Cr⁵¹-labeled T2 target cells was assessed using a chrome release assay as described previously (41).

Establishment of lymphoblastoid cell lines

Lymphoblastoid cell lines were established from PBMC of an HLA-A*0201 expressing donor by incubating 1×10^7 PBMC in RPMI 1640 medium containing 15% FCS and supplemented with cell-free supernatant of a mitogen-activated culture of B 95-8 cells containing high titers of EBV. Growing clones were expanded by splitting the cultures in corresponding intervals using RPMI 1640 medium with 10% FCS. All lymphoblastoid cell lines used for this study strongly expressed HLA-A2 molecules as assessed by flow cytometry.

Confocal microscopy and immunocytochemistry

Raji cells were pulsed with 10 μ g/ml SEA at 37°C for 30 min. CTL were incubated with Alexa⁴⁸⁸-labeled anti-CD3 mAb at 37°C for 30 min to label CD3-endo. CTL were mixed 1:1 with Raji cells and plated on poly-ornithine-coated glass coverslips and incubated at 37°C for 30 min (if not specifically mentioned in the figure legends). Samples were then fixed with ice-cold 4% paraformaldehyde for 20 min and processed for immunocytochemistry. LG were labeled with Alexa⁶⁴⁷-labeled anti-perforin mAb dG9. Polyclonal rabbit Vti1b Ab was used to stain endogenous Vti1b. Golgi was labeled with anti-GM130 Ab. Alexa⁵⁶⁸-labeled goat anti-rabbit or goat anti-mouse secondary Abs were used accordingly. Then the samples were washed, mounted, and kept at 4°C until scanning. Confocal microscopy was carried out on a Nikon E600 using a $\times 100$ objective. Serial confocal z-sections were taken at 0.2- μ m intervals for whole-cell analysis. ImageJ 1.37v software was used to generate merged images and projections of confocal sections.

Epifluorescence deconvolution microscopy and time-lapse imaging

Four-dimensional (4D) fluorescence microscopy was performed with a Zeiss Cell Observer HS system with a $\times 100$ α Plan-Fluar Objective (N.A. 1.45) and an AxioCam MRm Rev. 3. To acquire the images as fast as possible, the cells were scanned with binning 3×3 and a z step size of 1 μ m. For fixed cells, images were acquired with binning 1×1 and a z step size of 0.2 μ m. Constrained iterative deconvolution was performed using a point spread function calculated with the z-stack acquisition from 170-nm yellow-green, orange, or deep-red fluorescent beads (PS-Speck; Invitrogen) using 30–40 iterations.

Evanescent-wave imaging and TIRF-based exocytosis

The TIRF setup was as described previously (43) with the following additions: a solid-state laser 85 YCA emitting at 561 nm (Melles Griot), a dual-view camera splitter (Visitron) to separate the red and green channels, and a Visichrome Monochromator (Visitron) to acquire images in epifluorescence. Human CTL overexpressing perforin–mCherry were settled for 2 min on anti-CD3/anti-CD28 Ab-coated coverslips. Cells were imaged for 30 min by TIRF microscopy. Following each TIRF image, three images were acquired as epifluorescence stacks with a z step size of 0.5 μ m, the first epifluorescence plane being at the same plane as that of TIRF microscopy. The acquisition speed was 1 Hz, and the exposure time was 100 ms.

The movement of a single granule was monitored as follows: Metamorph version 6.3 was used to analyze the movement/secretion of LG at the IS. Every slice of the TIRF video after background correction was checked carefully for secretion (meaning to check if vesicle fluorescence was lost in

the TIRF picture). The time interval between each slice of the TIRF video was 1 s, and within that 1 s three images in epifluorescence were also taken at different planes. One second of one experiment therefore generated four time-lapse movies, one being at the TIRF plane and another epifluorescence image in the same plane. The other two epifluorescence images were taken at one or two planes higher than the first plane (step size was 500 nm). When a vesicle that was present in one slice disappeared in the next slice (1 s later), a region of interest was made circling that particular vesicle just before it disappeared. The same region of interest was copied and pasted onto the three epifluorescence images. If the vesicle had been secreted, it did not appear in any of the subsequent epifluorescence images. However, if the vesicle had moved back into the cytosol, then it did appear 1 s later in either one of the two planes that are higher than the TIRF plane.

siRNA treatment

SEA-specific CTL were transfected with siRNA using a nucleofector kit (Lonza) according to the manufacturer's instructions. The following siRNAs were used: vti1b siRNA [VTi1B_8_4479, Qiagen; modified by Qiagen as described by Mantei et al. (44)], stx11 siRNA (1642453; Qiagen), and stx6 siRNA (L-017164-00; Dharmacon). A modified nonsilencing siRNA (Qiagen) was used as control.

Quantitative real-time polymerase chain reaction

Quantitative real-time PCR (qRT-PCR) was carried out in a MX3000 instrument from Stratagene. Primers were designed using the Primer3 program (45) available at <http://frodo.wi.mit.edu/>. PCR fragments were confirmed by sequencing (MWG). Expression of *vti1b* was normalized to the average expression of the housekeeping genes *RNA Polymerase II*, *TATA box-binding protein*, and *ARF1*.

Western blot

CTL were collected 36 h after siRNA transfection. Equivalent amounts of proteins were separated by 12–14% SDS-PAGE and transferred to nitrocellulose membrane using a transblot electrophoresis transfer cell (Fisherbrand). ECL reagent (Amersham) was used for immunoblot detection.

Single-cell Ca^{2+} imaging

Ca^{2+} imaging was performed as described in Ref. 43. Raji target cells were pulsed with 10 μ g/ml SEA at 37°C for 30 min, washed twice, and resuspended in Ca^{2+} Ringer's solution. Raji cells were added to the chamber at $t = 0$ s onto the CTL. Ca^{2+} signals were analyzed of CTL that showed a clear contact with a target cell in infrared images. Control experiments were performed after addition of Raji cells not pulsed with SEA.

Cytotoxicity assay

The CytoTox 96 Non-Radioactive Cytotoxicity Assay (Promega) was used to detect target lysis. CTL were plated in 96-well plates in AIMV medium (5% FCS) with 1×10^4 SEA-pulsed Raji target cells at various effector/target ratios. CTL and target cells were incubated at 37°C for 4 h, and then the lactate dehydrogenase activity in the supernatant was measured. The cells were pelleted at $200 \times g$ for 4 min. Then, 50 μ l supernatant was taken from each well and incubated with the reaction substrate for 30 min at room temperature. The absorbance was measured at 490 nm with the GENios Pro plate reader (TECAN). Cytotoxicity was calculated with the following equation: % cytotoxicity = (experimental – effector spontaneous – target spontaneous)/(target maximum – target spontaneous) \times 100. All cytotoxicity assays were done in triplicate.

LG accumulation analysis

The analysis of LG accumulation was performed with Metamorph version 6.3. The raw data stacks were first corrected for background, and then a threshold value was set for every cell such that only the pixels above a given fluorescence intensity that mark the LG were selected. The value of the pixels defined as the threshold area was obtained for every frame of the time lapse video for each individual cell. Because of difficulties in tracking every single vesicle for all the cells, a ratio was made between the threshold area and number of vesicles for a minimum of three frames for every cell. The area threshold was then divided by this ratio for all the time frames to get the number of vesicles for each frame. The average of the number of vesicles was then plotted against the time in seconds.

Automated analysis of pairing

It was performed with AxioVision (Carl Zeiss). First, the three-dimensional reconstruction was generated from the whole stack for each sample. Af-

terwards, the boundaries of LG (or CD3-endo) were automatically defined by the *Measure 3D* with the default threshold. Then the following parameters were obtained (by *Selective 3D Measurement*): the x , y , and z coordinates of the center of gravity of the granules/vesicles, as well as the length of the major axis of the granules/vesicles. The distance (D) of LG and CD3-endo was calculated (center to center) as follows: $D = \sqrt{[(X_{LG} - X_{CD3})^2 + (Y_{LG} - Y_{CD3})^2 + (Z_{LG} - Z_{CD3})^2]}$. The distances of each LG to all the CD3-endo were calculated. Then D was compared with the sum of major axis of the corresponding LG and CD3 endosome ($M_{LG} + M_{CD3}$). If $D \leq M_{LG} + M_{CD3}$, this LG is considered to pair with the corresponding CD3 endosome. No matter how many CD3-endo the LG is paired with, this LG is counted only once as a paired LG. The pairing rate is calculated as: (number of paired LG/number of total LG) \times 100%.

For TIRF images, pairing was examined in two dimensions. The distance (D) of LG and CD3-endo was calculated (center to center) as follows: $D = \sqrt{[(X_{LG} - X_{CD3})^2 + (Y_{LG} - Y_{CD3})^2]}$. The distances of the afterward released LG to all the CD3-endo were calculated. Then D was compared with the sum of major axis of the corresponding LG and CD3 endosome ($M_{LG} + M_{CD3}$). If $D \leq M_{LG} + M_{CD3}$, this LG is considered to pair with the corresponding CD3 endosome.

Computation of the pairing probabilities for random vesicle configurations

We implemented a Monte Carlo algorithm to generate stochastically vesicle configurations within a given volume. The test volume was a spherical shell with inner radius r_i reflecting the large nucleus of the cell (which has to be excluded as an area of vesicle location) and outer radius r_a . Generally, we set for a given outer radius r_a the inner radius to $r_i = 0.8 r_a$, which is from our experience an upper limit for the size of the nucleus (if we assume a smaller nucleus, the random pairing probability would be even smaller). We performed several simulations with different outer radii r_a between 4 μ m and 6 μ m and different radius R of the individual vesicles (green for CD3-endo and red for LG) between 0.1 μ m and 0.5 μ m. The number of CD3-endo, N , was varied from 1 to 60, and the number of LG, M , was fixed to be 18, which is the average number of LG that we measured in resting CTL. The random pairing probability for LG depends of course on the number of CD3-endo N but not on the number of LG M (which means that results are independent of the number of LG we assume for the simulation). For each parameter set (r_a, R, N) the probability for a LG to pair with one of the N CD3-endo was calculated by stochastically generating a large number (100,000) of green and red vesicle configurations within the allowed volume.

This was done by using a pseudo-random number generator (ran3.c from Ref. 46) to generate spatial coordinates (x, y, z) of the vesicle centers with $0 < x < r_a$, $0 < y < r_a$, and $0 < z < r_a$. The N coordinates (x_n, y_n, z_n) ($n = 1, \dots, N$) of the CD3 endosome centers were accepted if they were within the allowed spherical shell, that is, $r_i^2 < x_n^2 + y_n^2 + z_n^2 < r_a^2$ and the corresponding vesicles with radius R were non-overlapping, that is, $(x_n - x_m)^2 + (y_n - y_m)^2 + (z_n - z_m)^2 > (2R)^2$ for all pairs (n, m) of vesicle coordinates. After the construction of a feasible CD3 endosome configuration, the LG coordinates were generated in the same way. This gave one allowed vesicle configuration sample, which was tested for pairing: for each LG with coordinates (x, y, z), we tested whether there was at least one CD3 endosome with coordinates (x', y', z') with $(x - x')^2 + (z - z')^2 + (z - z')^2 < (2R)^2$. The number of paired LG divided by the total number of LG gave the pairing probability for the specific sample under consideration; averaging this number over 100,000 samples gave the estimate for the pairing probability for the given set of parameters (r_a, R, N) and its statistical error via mean square deviation from the mean. The latter was smaller than the point size in Supplemental Fig. 1B–D. The percentage of paired LG is 100 times this pairing probability.

The compartment model

The changes of the different populations are described by

$$\frac{dS}{dt} = k_1 - k_2S - k_4S + k_5SM \quad (1)$$

$$\frac{dP}{dt} = k_2S - k_3P \quad (2)$$

$$\frac{dSM}{dt} = k_4S - k_5SM \quad (3)$$

$$\frac{dPM}{dt} = k_3P - k_6SM \quad (4)$$

$$\frac{dR}{dt} = k_6 PM, \quad (5)$$

where SM is the single LG in proximity to the IS; PM is the paired LG in proximity to the IS; S is the single LG in the rest of the CTL; P is the paired LG in the rest of the CTL; and R is the released LG. For fixed rate constants k_1, \dots, k_6 , equations 1–5 were numerically integrated using a fourth order Runge–Kutta method, and the rate constants were then fitted to give the best agreement between the predicted time evolution of the vesicle populations with the measured experimental data.

Data analysis

Data were analyzed using ImageJ 1.37v, Metamorph (Visitron), AxioVision (Zeiss), Igor Pro (Wavemetrics), Microsoft Excel, and SigmaPlot 8.0. All values are given as mean \pm SEM if not mentioned otherwise, and $*p < 0.05$, $**p < 0.01$, and $***p < 0.001$ by Student t test. If data points were normally distributed, an unpaired two-sided Student t test was used. If normal distribution could not be confirmed, a nonparametric test (Mann–Whitney) was performed.

Results

CTL polarization: MTOC relocates toward the IS in human CTL

Polarization of organelles and molecules is a key process during formation of the IS. The MTOC and Golgi apparatus have been shown to relocate to the IS (4, 47, 48). As cytoskeletal structures and the MTOC are critically involved in LG delivery to the IS (19, 23), we confirmed their polarization in CTL under our experimental conditions. Fig. 1A shows polarization of the MTOC and Golgi toward the IS in activated primary human CD8⁺ T cells. Seventy-seven percent of the cells ($n = 25$) showed a clear polarization of the MTOC and Golgi to the IS, where polarization was defined as accumulation within a segment encompassing one third of the cell's diameter and thus representing 25.9% of the cell volume (Fig. 1B). Our findings are similar to the data obtained by Stinchcombe et al. (23) in mouse CTL and by Orange et al. (19) in NK cells and confirm cytoskeleton-dependent polarization in CTL. Live cell imaging revealed the kinetics of MTOC translocation toward the IS within the first few minutes after target cell contact in 96% of the analyzed cells ($n = 50$) (Fig. 1C). To visualize the MTOC localization directly at the IS, we used TIRF microscopy, which allows exclusive visualization of fluorescence within 200 nm of the IS. A functional IS was formed between CTL and anti-CD3/anti-CD28 Ab-coated glass coverslips (43). As expected, we observed accumulation of LG at the IS in the TIRF plane over extended times, indicating stable LG docking, which is defined as the close apposition of organelles at the plasma membrane of the IS (35, 36). However, we did not usually observe the appearance of the MTOC in the TIRF plane in human CTL during the whole experiment (8 of 11 cells). Rather, we regularly observed the MTOC in the epifluorescence picture taken 0.5 μm away from the IS (Fig. 1D). These experiments suggest that, in contrast to the electron microscopy experiments in mouse CTL, in which the MTOC has been shown to touch the plasma membrane to deliver LG to the IS (23), in human CTL, the MTOC is unlikely to be involved in the docking of LG at the plasma membrane at the IS. To understand how LG could potentially dock at the plasma membrane within the IS, we designed experiments to analyze the transport and subcellular localization of LG in CTL after target cell contact.

LG are tethered with TCR-containing endosomes

Confocal microscopy was used to investigate CTL with and without target cell contact. LG were stained with the anti-perforin Ab dG9, which labels only mature perforin. CD3 was used as a marker to examine TCR enrichment at the IS. Analyzing the localization of

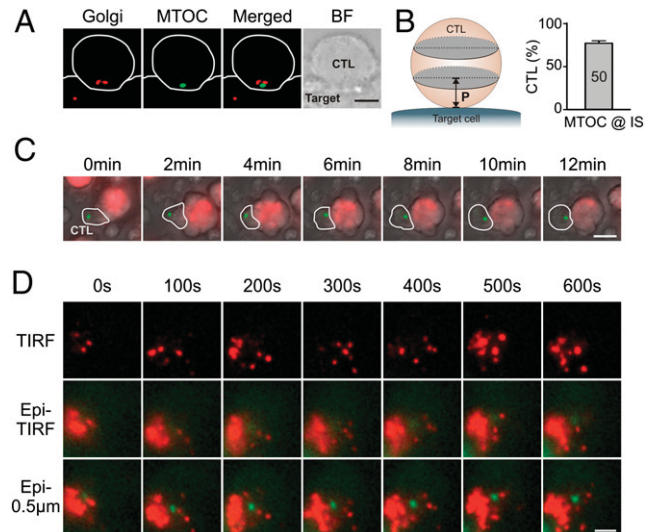


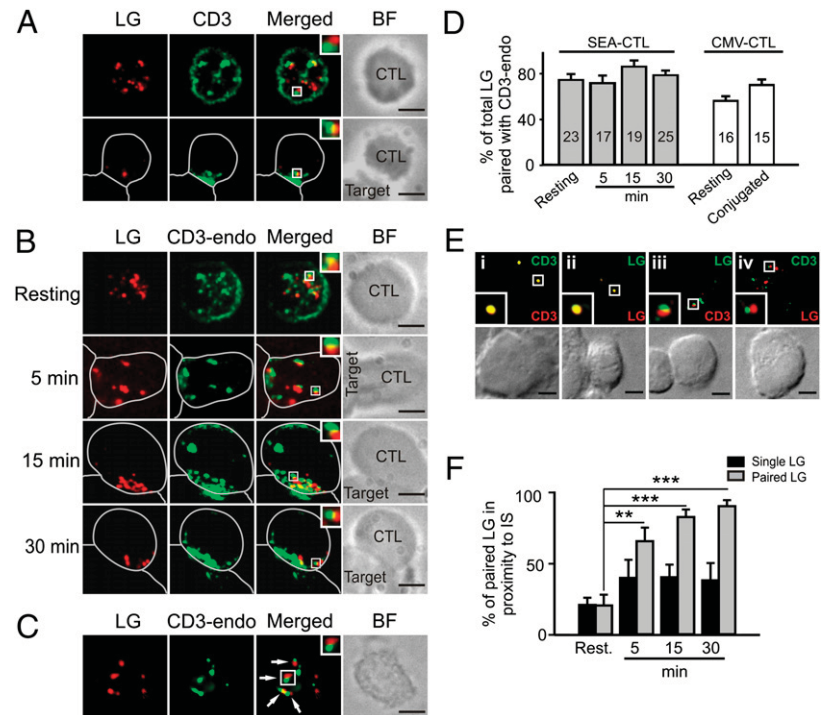
FIGURE 1. MTOC does not directly mediate LG docking at the plasma membrane. **A**, MTOC and Golgi apparatus are polarized to the IS. CTL were incubated with SEA-pulsed Raji cells at 37°C for 30 min and fixed with ice-cold 4% paraformaldehyde. MTOC was labeled with γ -tubulin–GFP. Golgi was labeled with anti-GM130 Ab. The samples were analyzed by epifluorescence deconvolution microscopy. Scale bar, 3 μm . **B**, Quantification of MTOC polarization in conjugated CTL. The region from the contact interface up to one third of the diameter of the CTL was defined as proximity to the IS (P). MTOC was considered to be polarized when MTOC was present in region P. **C**, Time-lapse imaging of MTOC translocation to the IS. MTOC was labeled as described in **A**. Target cells were prepulsed with SEA and were additionally loaded with fura 2-AM to identify them (pseudocolored in red). Live cell imaging was carried on at 37°C, with 5% CO₂. Scale bar, 10 μm . **D**, MTOC is polarized to the IS but does not directly contact the plasma membrane. MTOC was labeled as described in **A**. Perforin–mCherry was used to label LG. Glass coverslips were coated with anti-CD3/anti-CD28 Ab. Epifluorescent images were taken both at the TIRF plane and 0.5 μm above the TIRF plane. Scale bar, 3 μm .

LG and CD3-endo in more detail, we were surprised to find that many LG and TCR were localized next to each other in resting (no target cell) and activated (with target cell contact) CTL (Fig. 2A). We refer to this close apposition of LG and TCR as being paired or tethered.

To distinguish whether LG are tethered with newly synthesized CD3 or already existing CD3, we labeled membrane and endocytosed CD3 with Alexa⁴⁸⁸-conjugated anti-CD3 Ab by a 30-min preincubation of the living cells. The Alexa⁴⁸⁸-conjugated anti-CD3 Ab was not dissociated from CD3 molecules after being internalized because we observed a perfect colocalization between the internalized Alexa⁴⁸⁸-conjugated anti-CD3 Ab and the Alexa⁶⁴⁷-conjugated anti-CD3 Ab staining after the fixation of the cells (Supplemental Fig. 1A). After T cell–target cell contacts were formed, prelabeled CD3 molecules and LG were enriched at the CTL–target cell contact over time (Fig. 2B), indicating that this labeling method does not compromise IS function. At all time points during IS formation, the tethering between LG and CD3-endo was observed (Fig. 2B, insets).

Because the concept of tethering has not been described for these different intracellular components, we designed experiments to examine this process rigorously. First, we analyzed the subcellular localization of LG and CD3-endo in a rather physiological scenario using *in vivo*-activated primary human CTL. We repeated the experiments with a CMV-specific T cell subpopulation enriched from donors. Again, we found that many LG and CD3-endo were localized next to each other in resting and conjugated CMV-specific

FIGURE 2. Tethering of LG and CD3-endo. **A**, LG (red) were labeled with Alexa⁶⁴⁷-labeled anti-perforin mAb. CD3 was stained with Alexa⁴⁸⁸-labeled anti-CD3 mAb. In both resting CTL and CTL in contact with target cells, LG were often found to be juxtaposed with CD3. **B**, To distinguish from newly synthesized CD3, already existing CD3 (CD3-endo) were labeled in live CTL by preincubating with Alexa⁴⁸⁸-labeled anti-CD3 mAb. LG were labeled with Alexa⁶⁴⁷-labeled anti-CD3 mAb. **C**, Same as in **B**, only that CMV-CTL were analyzed. The white arrows indicate LG/CD3-endo pairs. **D**, Quantification of pairing rate of LG with CD3-endo. Gray and open bars stand for SEA-CTL and CMV-CTL, respectively. **E**, CD3-endo were labeled with Alexa⁴⁸⁸-labeled anti-CD3 mAb in *i* and *iv* and with Alexa⁶⁴⁷-labeled anti-CD3 mAb in *i* and *iii*. LG were labeled with Alexa⁶⁴⁷-labeled anti-perforin mAb in *ii* and *iv*, as well as FITC-labeled anti-perforin mAb in *ii* and *iii*. Images were acquired with the Zeiss Cell Observer and were deconvolved. **F**, LG in proximity to the IS were analyzed at different time points after CTL contact with the target cell. Scale bars, 3 μ m. $n > 20$ cells were analyzed for each condition. ** $p < 0.01$, *** $p < 0.001$.



CTL, the latter of which were conjugated with CMV-peptide loaded B cells (Fig. 2C). We conclude that tethering between LG and CD3-endo is a common feature of primary human CTL. An automated analysis of pairing was performed, and the statistical analysis of tethering between LG and CD3-endo shows a very high percentage ranging from 60 to 90% for superantigen or CMV-Ag activated CTL (Fig. 2D).

Because LG and CD3-endo could also pair in a random manner, we performed a Monte Carlo simulation (as described in *Materials and Methods*) to estimate how high the random pairing should be. Depending on the parameters chosen for the simulation (for instance, radius of the cell = 5 μ m), random pairing was usually much smaller than 40% (Supplemental Fig. 1B–D).

Second, to exclude the possibility of colocalization between LG and CD3, LG and CD3 were each stained with two different Abs, and their localization was analyzed by epifluorescence deconvolution microscopy (Fig. 2E and Supplemental Fig. 1E–H). Fig. 2E depicts the double staining of CD3 with Alexa⁶⁴⁷- and Alexa⁴⁸⁸-conjugated anti-CD3 Abs (Fig. 2Ei), the double staining of LG with Alexa⁶⁴⁷- and FITC-conjugated anti-perforin Abs (Fig. 2Eii), and the two different combinations of single labeling of LG and CD3 (Fig. 2Eiii, 2Eiv). As expected, the double staining of only CD3 (Fig. 2Ei) or only LG (Fig. 2Eii) showed a clear colocalization. However, the two separate staining conditions of LG and CD3 (Fig. 2Eiii, 2Eiv) did not show colocalization but instead showed pairing of LG and CD3. We conclude that LG tether with CD3 and are not colocalized in the same compartment.

Third, to check whether the pairing between CD3-endo and LG was specific for CD3-endo, we compared the localization of LG and endocytosed transferrin receptors as a control. Transferrin is recycled through the constitutive recycling pathway (49, 50). Using Alexa⁴⁸⁸-conjugated transferrin to label recycling transferrin receptors (TfR), we observed only infrequent pairing between LG and the endocytosed TfR (Supplemental Fig. 2A), which was on average <30% in contrast to the 80% pairing between LG and CD3-endo (Supplemental Fig. 2B). Some TfR vesicles have been shown to colocalize with CD3-endo (12). We suggest that the few

TfR vesicles, which were tethered with LG, might share common features with CD3-endo or were randomly paired.

To characterize CD3-endo paired with LG, we analyzed paired CD3-endo with the established endosomal markers Rab5 (early endosome), Rab7 (late endosome), and Rab11 (recycling endosome). We found that $50.9 \pm 5.0\%$, $51.6 \pm 6.4\%$, and $37.4 \pm 5.2\%$ of paired CD3-endo are colocalized with Rab5, Rab7, and Rab11, respectively (Supplemental Fig. 2C), which suggests that CD3-endo can be paired with LG at all intracellular trafficking steps. It has been reported that Rab5 and Rab7 may overlap at some stage (51). Therefore, it is not surprising that the sum of percentage of paired CD3-endo, which were colocalized with Rab5, Rab7, and Rab11, is >100%. This may indicate that CD3-endo are also paired with LG at intermediate transition states. Additionally, we characterized the total CD3-endo population with the endosomal markers. As shown in Supplemental Fig. 2D, CD3 was partially colocalized with Rab5, Rab7, and Rab11. The Mander's correlation coefficients (M1: Rab in CD3) ranged from 0.31 to 0.35, indicating that after internalization, CD3 was transported to early, late, and recycling endosomes, and each type of endosome represents about one third of the total CD3-endo population.

To analyze the accumulation of LG at the IS in detail, we quantified the localization of single and paired LG at various time points after target cell recognition using the same cell partitioning as in Fig. 1B. We found that paired LG were significantly enriched at the IS up to ~90% over time compared with resting conditions, whereas no significant change in the localization of single LG was observed (Fig. 2F). These results imply that the probability of LG accumulation at the IS was increased by pairing LG with CD3-endo.

Fitting the data according to the compartment model (compare also in the *Discussion*) revealed that the rates of vesicle transport have to change between 5 and 10 min after synapse formation. The following rates were used to fit the data assuming a linear crossover from the rates at 5 min to the ones at 10 min (Table I). The LG release rate k_6 varies from 0.25 to 0.2 min^{-1} , implying a mean release time of 4–5 min for paired LG (Table I).

Table I. Rate constants of the compartment model as defined in *Materials and Methods* by equations 1–5

Time (min)	k_1 (min ⁻¹)	k_2 (min ⁻¹)	k_3 (min ⁻¹)	k_4 (min ⁻¹)	k_5 (min ⁻¹)	k_6 (min ⁻¹)
$t < 5$	0	0.2	0.3	3.2	5.6	0.25
$t > 10$	1.2	0.86	1.2	3.2	5.6	0.2

The model could only fit the data well if the transport rates k_1 to k_6 were changed between 5 and 10 min after target cell recognition. The model also shows that 10 min after target cell contact, the LG/CD3-endo pairing rate k_2 increases by a factor of four compared with the early IS formation phase (i.e., the first 5 min after CTL–target cell contact); and also k_3 , the rate of transport of paired LG to the IS, increases by a factor of four. In contrast, the rates k_4 and k_5 for the transport of single LG toward and away from the IS, respectively, remained unchanged. The model also predicts that 10 min after target cell contact, new LG are generated, as k_1 is increased. Up-to-date imaging approaches, without modifying the endogenous proteins, still cannot measure the LG generation in vivo. Our model reveals that after CTL form a contact with target cells, new LG are generated ($k_1 > 0$) to refill the cytotoxic granule pool and compensate for the released LG.

Finally, the model shows that LG can be released even at the early stage of IS formation, as $k_6 = 0.25 \text{ min}^{-1}$ and >4 paired vesicles at the IS imply the release of at least one LG per minute. Thus, our data and model predict that CTL can kill efficiently within a few minutes by the LG/CD3-endo pairing mechanism, which guarantees the rapid and efficient accumulation of LG at the IS.

Visualization of LG/CD3-endo transport to the IS by 4D imaging

To exclude that tethering between LG and CD3-endo is an artifact introduced by fixation, we visualized the movement of LG and CD3-endo in living cells using fast 4D fluorescence microscopy. CD3-endo were labeled with an Alexa⁴⁸⁸-conjugated Ab against CD3, and LG were labeled by overexpressing perforin tagged with mCherry (perforin–mCherry). Perforin–mCherry colocalized very well with the dG9 anti-perforin Ab, indicating its correct localization in perforin-containing LG (Supplemental Fig. 3A). Paired LG/CD3-endo were cotransported to the IS formed between CTL and the target cell (located in Fig. 3A, lower right corner) and Supplemental Video 1). After LG/CD3-endo pairs reached the IS, $>80\%$ of these LG/CD3-endo pairs remained at the IS for $>30 \text{ s}$. In some CTLs, single LG were also transported to the IS. However, 30 s after approaching the IS, only 20% of these single LG still remained at the IS (Fig. 3B). These data illustrate that LG/CD3-endo pairs can be transported together, and paired LG can reside longer at the IS than single LG. This implies that the in-

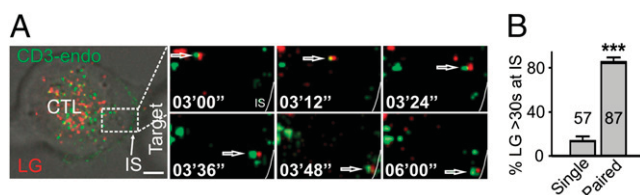


FIGURE 3. Cotransported LG and CD3-endo accumulate at the IS. *A*, LG and CD3-endo are cotransported to the IS. CTL overexpressing perforin–mCherry were incubated with Alexa⁴⁸⁸-labeled anti-CD3 mAb to label CD3-endo. Scale bar, 3 μm . *B*, The percentage of single ($n = 57$) or paired LG ($n = 87$) that remained at the IS $>30 \text{ s}$. *** $p < 0.001$.

teraction between LG and CD3-endo increases the dwell times of LG at the IS, suggesting that the tethering might be important for docking of LG at the IS.

TIRF microscopy reveals the functional importance of LG/CD3-endo pairs for LG docking and release

To confirm further LG/CD3-endo pairing and test its functional importance at the IS, we analyzed LG and CD3-endo by TIRF microscopy, which allows exclusive visualization of granules within 200 nm of the IS. To apply TIRF microscopy, a functional IS was formed between CTL and anti-CD3/anti-CD28 Ab-coated glass coverslips. The immobilized anti-CD3/anti-CD28 Abs induce a functional IS between coverslip and CTL, because Ca^{2+} influx was initiated (43), cell polarization was induced (Fig. 1D), actin accumulated at the IS and segregated into a ring like structure (A. Quintana, C. Junker, and M. Hoth, unpublished observations), and LG were secreted (see later). We used anti-CD3/anti-CD28 coating instead of only anti-CD3 because we found a better LG accumulation with costimulation. We found that most LG reached the IS while being paired to CD3-endo (Fig. 4A and Supplemental Video 2), which is in agreement with our data from live-cell imaging and the confocal microscopy. Comparing the dwell times of paired and single LG at the IS, we found that paired LG remained significantly longer at the IS than single ones (Fig. 4B), which is in agreement with Fig. 3B. To assess the influence of pairing on LG release, we established an assay to analyze the exocytosis of LG with TIRF microscopy (Fig. 4C and Supplemental Video 3). In addition to the TIRF plane, three consecutive epifluorescence images in the z -dimension were acquired to resolve areas of the cell with greater distance from the IS. A vesicle disappearing from the TIRF plane was thus classified as secreted if it could not be seen in the other planes at the corresponding position (Supplemental Fig. 3B). A vesicle that moved from the TIRF plane to the adjacent planes was classified as

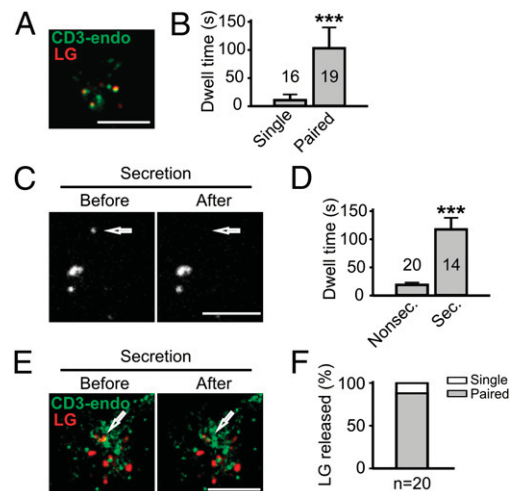


FIGURE 4. TIRF microscopy analysis of paired vesicles revealed that tethering with CD3-endo increases docking of LG at the IS and thus enhances LG release. *A*, Example of TIRF microscopy image of paired LG/CD3-endo at the IS formed between CTL and anti-CD3/anti-CD28 Ab-coated glass coverslips. CTL overexpressing perforin–mCherry (LG, red) were incubated with Alexa⁴⁸⁸-labeled anti-CD3 mAb to label CD3-endo. *B*, Dwell times of single and paired LG at the IS. *C*, Example of an LG secretion event at the IS. LG were labeled with overexpressing perforin–mCherry. *D*, Dwell times of nonsecreted (Nonsec.) and secreted LG (Sec.) at the IS. *E*, Secretion of an LG (red) paired with CD3-endo. *F*, Analysis of the relative proportion of single and paired LG release at the IS. Scale bars, 3 μm . *** $p < 0.001$.

having moved back from the IS into the cytosol (Supplemental Fig. 3C). In addition, we used a LAMP-1 degranulation assay similar to that of Ref. 33 to test TIRF-based LG exocytosis. Anti-CD3/anti-CD28 Ab coating used for TIRF experiments can efficiently induce vesicle release comparable with that of studies using other stimuli (52, 53).

Using the TIRF approach, we quantified the average dwell times of the secreted and nonsecreted LG. Dwell times of secreted LG were drastically increased compared with the dwell times of nonsecreted LG implying that secreted LG were docked at the plasma membrane before their release (Fig. 4D). Dwell times of LG/CD3-endo pairs were similar to those of secreted LG, whereas the dwell times of single granules were comparable with the dwell times of nonsecreted LG (compare Fig. 4B and 4D). This suggests that mainly paired LG were secreted. To test this hypothesis more directly, we compared the release of paired and unpaired LG. Pairing was analyzed again using the described automated routine. Fig. 4E illustrates the release of a paired LG (see also Supplemental Video 4). On average, 88% of the released LG were paired (Fig. 4F) and within the first 7 min of IS formation, all secreted LG were paired with CD3-endo. We therefore conclude that the pairing of LG with CD3-endo is responsible for enhancing their dwell times at the IS, which very likely represents vesicle docking, a prerequisite to increase their release efficiency.

The SNARE protein Vti1b is involved in the tethering between LG and CD3-endo

An important question is which molecules mediate the tethering between LG and CD3-endo. Because proteins of the SNARE superfamily play a central role in budding, target selection, and fusion of intracellular compartments (34–36), we analyzed their potential involvement in LG/CD3-endo tethering. We screened many different SNARE proteins for their subcellular localization and found that the Qb-SNARE protein Vti1b is specifically colocalized with both LG and CD3-endo and accumulates at the IS after CTL contact with target cells (Fig. 5A), suggesting that Vti1b might play a role in pairing of LG with CD3-endo.

We tested the importance of Vti1b using RNA interference technology. A recently reported modification of siRNA can efficiently downregulate protein expression in primary T cells (44). Introducing this modification into Vti1b-siRNA, we were able to efficiently downregulate Vti1b in activated primary human CD8⁺ T cells as confirmed by qRT-PCR (Fig. 5B) and Western blot (Fig. 5C) compared with control siRNA. Vti1b downregulation correlated with a decrease of the LG/CD3-endo pairing rate. The number of paired LG was reduced in Vti1b downregulated CTLs by 50% compared with control CTL, and the number of single LG was increased accordingly (Fig. 5D, 5E), whereas the total number of LG (Fig. 5E) and CD3-endo (Supplemental Fig. 4A) remained unchanged. To examine whether the tethering is particularly Vti1b-dependent, we analyzed the potential role of another SNARE protein, syntaxin 11 (Stx11), in tethering. Stx11 is involved in the killing mechanism (31), and a recent report shows that Stx11 interacts with Vti1b in macrophages (54). After the downregulation of Stx11 by siRNA, we found in contrast to Vti1b downregulated CTL no change in tethering in Stx11 downregulated CTL compared with control CTL (Supplemental Fig. 4B). The downregulation of Stx11 was confirmed at the mRNA and protein level (Supplemental Fig. 4C, 4D). In summary, our data show that Vti1b is involved in the tethering between LG and CD3-endo.

Next we analyzed the functional implications of Vti1b downregulation by confocal microscopy. In nonsilencing siRNA transfected cells, the typical enrichment of CD3-endo and LG at the

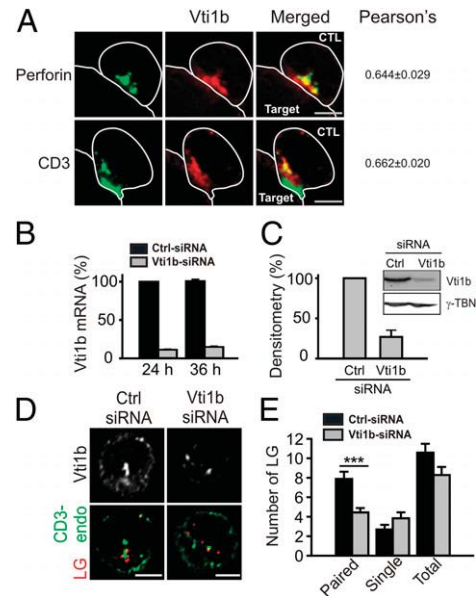


FIGURE 5. Vti1b is required for pairing LG and CD3-endo. **A**, Colocalization of Vti1b with LG and CD3-endo. CTL were incubated with SEA-pulsed Raji cells and fixed with ice-cold 4% paraformaldehyde. LG were labeled with Alexa⁶⁴⁷-labeled anti-perforin mAb. To label CD3-endo, CTL were preincubated with Alexa⁴⁸⁸-labeled anti-CD3 mAb at 37°C for 30 min. A polyclonal rabbit anti-Vti1b Ab was used to stain endogenous Vti1b. Pearson's coefficients were analyzed with ImageJ. Thirty-one cells for each case were used. **B** and **C**, Vti1b expression after siRNA transfection was analyzed at the mRNA level by qRT-PCR (**B**) and on protein level by Western blot (**C**). A nonsilencing siRNA was used as the control for Vti1b-siRNA. **D** and **E**, Downregulation of Vti1b correlated with a lower pairing rate. CTL were preincubated with Alexa⁴⁸⁸-labeled anti-CD3 mAb at 37°C for 30 min to label CD3-endo. LG were labeled with Alexa⁶⁴⁷-labeled anti-perforin mAb. Polyclonal rabbit Vti1b Ab was used to stain endogenous Vti1b. The statistical analysis of **D** is shown in **E**. Scale bars, 3 μm. $n > 20$ cells were analyzed for each condition. *** $p < 0.001$.

IS was observed (Fig. 6A). In Vti1b-siRNA transfected CTL, however, LG still remained scattered all over the CTL even 30 min after target cell contact, and the number of LG in proximity to the IS was reduced, whereas CD3-endo could still be enriched at the IS similar to control CTL (Fig. 6A, 6B). However, MTOC and Golgi polarization to the IS (Fig. 6C) and TCR-activated Ca²⁺ influx (Fig. 6D, 6E), which is required for LG secretion (18, 26, 55), remained unchanged in Vti1b downregulated CTL. These experiments indicate that the signaling downstream of TCR and the general CTL polarization mechanisms during IS formation are normal in Vti1b downregulated CTL. Thus, the reduction of LG accumulation at the IS in Vti1b-siRNA transfected cells is not linked to a general T cell polarization failure or signaling defect but rather to the specific impairment in LG/CD3-endo pairing.

To test the importance of Vti1b in LG accumulation, we quantified the number of LG at the IS with TIRF microscopy in Vti1b-siRNA transfected CTL and nonsilencing siRNA transfected CTL (Fig. 7A). Similar to the data from fixed cells, we found a drastic reduction of LG numbers at the IS in Vti1b downregulated CTL compared with control CTL (Fig. 7A, 7B). Consequently, CTL-mediated cytotoxicity was also reduced by Vti1b downregulation (Fig. 7C). However, when the SNARE protein Stx6 (which is not colocalized with either CD3 or perforin based on unpublished observations by B. Qu, V. Pattu, S.S. Bhat, E.C. Schwarz, J. Rettig, and M. Hoth) was downregulated, CTL-mediated cytotoxicity was almost unaffected (Fig. 7D). The downregulation of Stx6 was confirmed by Western blot (Fig. 7E).

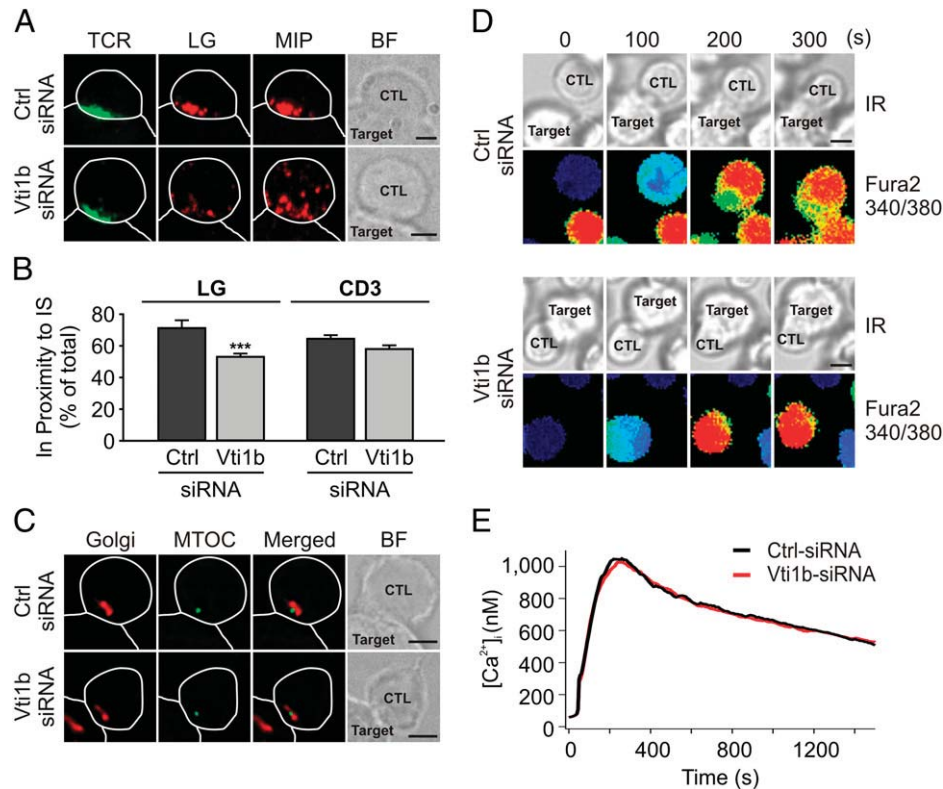


FIGURE 6. LG accumulation is inhibited by Vti1b downregulation, whereas T cell polarization and Ca^{2+} signaling are unchanged. **A**, LG accumulation at the IS was blocked by downregulation of Vti1b. LG and CD3-endo were stained as in Fig. 5A. CTL were transfected with Vti1b-siRNA or nonsilencing control siRNA. Thirty-six hours after transfection, CTL were used for experiments. The samples were scanned by confocal microscopy. MIP, maximum intensity projection. Scale bars, 3 μm . **B**, Quantification of accumulation of LG and CD3 at the IS from **A**. *** $p < 0.001$. **C**, Polarization machinery remains unchanged after Vti1b-downregulation. MTOC was labeled with overexpressing γ -tubulin-GFP. Golgi was labeled with anti-GM130 Ab. The samples were scanned by epifluorescence deconvolution microscopy. Out of three independent experiments, in 72% of nonsilencing siRNA transfected CTL ($n = 25$) and 68% of Vti1b-siRNA transfected CTL ($n = 19$), MTOC and Golgi apparatus were polarized as shown in **C**. Scale bars, 3 μm . **D**, Infrared (IR) and 340 nm/380 nm fura-2 ratio pictures of representative CTL transfected with either nonsilencing (Ctrl) siRNA or siRNA targeted against vti1b. Warmer colors indicate higher ratios. Different time points show CTL before and after contact with an SEA-pulsed Raji cell. CTL show an increase in $[\text{Ca}^{2+}]_i$ only after contact with a pulsed target cell. Cells with no contact showed no $[\text{Ca}^{2+}]_i$ increases (data not shown). Scale bars, 5 μm . **E**, Average $[\text{Ca}^{2+}]_i$ of CTL transfected with nonsilencing siRNA ($n = 194$) or siRNA against vti1b ($n = 273$). $[\text{Ca}^{2+}]_i$ signals after contact with SEA-pulsed Raji cells are unchanged in Vti1b-downregulated CTL.

Taken together, these data indicate that Vti1b is important for tethering of LG and CD3-endo, the accumulation, docking, and release of LG at the IS, as well as the consequential CTL-mediated cytotoxicity. These data also show that CD3-endo localizes at the IS independently of its juxtaposition to LG, but that LG requires tethering with CD3-endo to accumulate and dock at the IS (Fig. 8).

Discussion

Our data show that the tethering/pairing of LG and CD3-endo is required for efficient CTL-mediated target cell killing. The Qb-SNARE protein Vti1b is necessary for tethering between LG and CD3-endo, which explains its role in CTL-mediated cytotoxicity (33). The close interaction between LG and CD3-endo is required for the accumulation, docking, and secretion of LG at the IS. Vti1b downregulation by RNA interference decreased the probability of tethering between LG and CD3-endo. As a result, LG accumulation, docking, and release at the IS were impaired leading to a reduction in CTL-mediated cytotoxicity.

Griffiths and coworkers (23) have reported that MTOC polarization plays an important role in delivery of LG to the IS. Furthermore, Beal et al. (26) have found that MTOC is essential for the fast pathway to deliver LG to cSMAC. Very recently, Jenkins et al. (25) have shown that efficient MTOC polarization to the

cSMAC can be elicited by both strong and weak TCR signals, whereas LG are not accumulated at the IS in case of low TCR signals. Taken together, this indicates that MTOC polarization is required, but not sufficient, for LG reorientation at the IS. We found that MTOC is translocated to the IS but it rarely came in contact with the plasma membrane, indicating that MTOC is not responsible for docking LG at the plasma membrane at the IS, which is the prerequisite for granule release. The CD3-endo-dependent accumulation of LG reported by us may also facilitate the simultaneous enrichment of LG at two simultaneously formed IS, which has been observed by others (56) and us (Supplemental Fig. 4E). Enrichment of LG at two simultaneously formed IS require a docking mechanism independent of MTOC relocation.

TCR clustering and LG accumulation at the IS are two hallmarks of IS formation in CTL. It has been shown that despite MTOC translocation toward the IS in case of weak TCR signals (25, 57), both TCR enrichment (57) and LG accumulation (25) at the IS are substantially impaired. However, no direct link between TCR enrichment and LG accumulation has been reported before. We found that tethering between LG and CD3-endo is required for increased dwell times and release at the IS. This suggests that tethering with CD3-endo is required to dock LG at the plasma membrane. When TCR are not enriched at the IS after weak TCR signals (57), LG are also not accumulated at the IS. MTOC

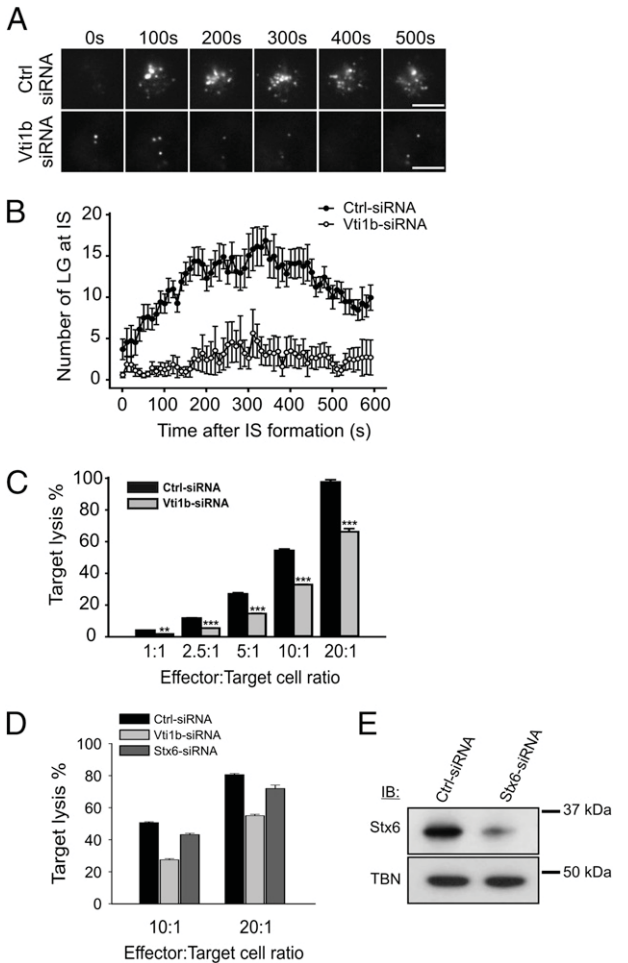


FIGURE 7. Vti1b-dependent LG/CD3-endo tethering is required for LG accumulation, docking, and CTL-mediated cytotoxicity. *A* and *B*, TIRF microscopy analysis after Vti1b downregulation compared with non-silencing control siRNA. CTL were transfected with Vti1b-siRNA or nonsilencing siRNA and perforin-mCherry constructs. The cells were used for TIRF microscopy 36 h after transfection. Scale bars, 3 μ m. *B*, The quantification analysis of LG accumulation. The TIRF images were acquired every 1 s for 600 s. The numbers of LG shown in the TIRF plane were quantified. Solid circles, nonsilencing control siRNA; open circles, Vti1b-siRNA. *C*, CTL-mediated cytotoxicity was impaired by downregulation of Vti1b. SEA-specific CTL and SEA-pulsed Raji cells were cocultured for 4 h at various effector/target cell ratios. Each condition was done in triplicate. One representative experiment out of three independent experiments is shown. Error bars show SD. $**p < 0.01$, $***p < 0.001$. *D*, CTL-mediated cytotoxicity was almost unaffected by Stx6 downregulation. One representative experiment out of three independent experiments is shown. Error bars show SD. *E*, Downregulation of Stx6 was confirmed by Western blot.

reorientation, however, is not impaired (25). If the tethering between LG and CD3-endo is disrupted, LG are not polarized toward the IS, despite the normal CD3-endo enrichment (Fig. 6*A*). In conclusion, tethering with CD3-endo is necessary for docking and release of LG at the IS.

Recently, the concept of organelle tethering has gained much attention since de Brito and Scorrano (58) showed that mitofusin 2 tethers the endoplasmic reticulum to mitochondria, which facilitates efficient mitochondrial Ca^{2+} uptake. We screened the literature for images of other potentially tethered organelles and found hints for paired vesicles in macrophages, mouse embryonic fibroblasts, and NRK fibroblast cells (59–61). Recently, tethering-like structures were observed also in NK cells (3).

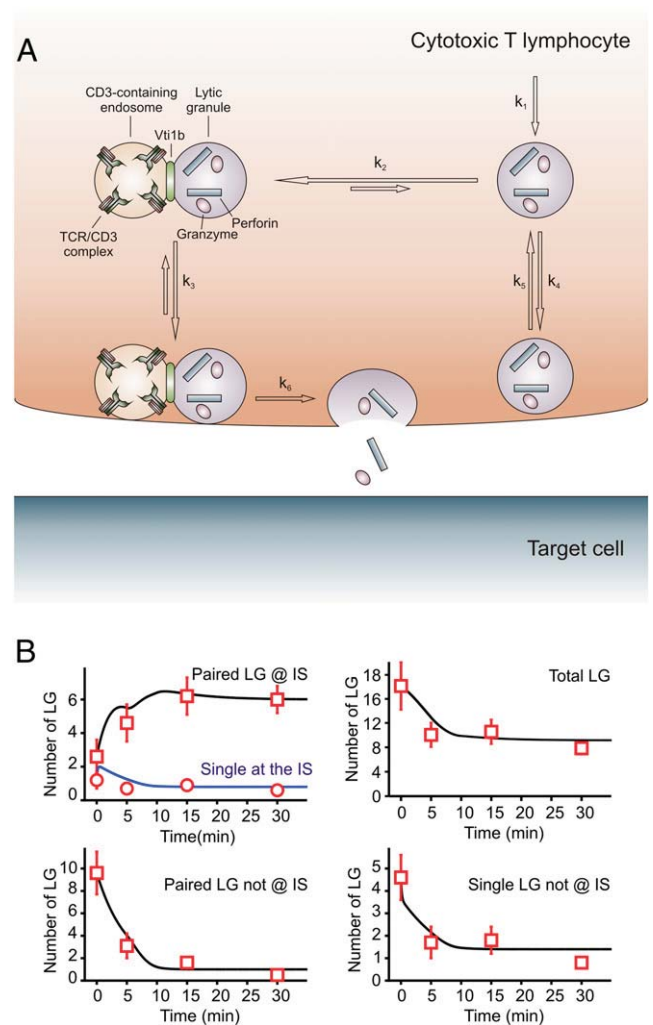


FIGURE 8. A compartment model for single and paired LG. *A*, A compartment model for single and paired LG. k_1 is the rate of perforin granule production. k_2 is the rate of formation of paired vesicles. k_3 is the rate of movement of paired vesicles to the IS. k_4 is the rate of single vesicles moving to the IS. k_5 is the reverse rate of k_4 . k_6 is the rate of paired vesicle release. *B*, The predicted curves according to the model (solid lines) fit the experimental results that were obtained from confocal experiments such as the one shown in Fig. 2*B*.

Ménager et al. (62) reported that the cytotoxic function of CTL required the Munc13-4-mediated cooperation of cytotoxic granules and Rab11-positive endosomal “exocytic vesicles.” Their work highlights the Rab11-mediated recycling pathway for the maturation of cytotoxic granules. Our work further verifies that endosomes—in particular, CD3-endo—play a pivotal role in LG release at the IS by tethering with LG and stabilizing them at the IS, thereby enhancing the LG release probability. In Munc13-4-deficient CTL, it is shown that LG are still reoriented to the IS but cannot be released (62). In Vti1b-downregulated CTL, LG cannot accumulate at the IS because of the impairment in tethering with CD3-endo. These findings suggest that the Vti1b-mediated interaction between LG and CD3-endo is located upstream of Munc13-4.

Whether LG and CD3-endo are localized in two different compartments that are tethered together or contained in different “subcompartments” of a larger organelle cannot be resolved by fluorescence microscopy. Notably, Peters et al. (16) showed more than 20 years ago that endocytosed TCR can be associated with the membranes of LG. They found that CD3 and CD8 can be

associated with the LG membrane but that their localization was distinct from the dense core of the vesicle, which most likely contains perforin. This suggests that TCR can be sorted into the LG but that it is in a subcompartment distinct from perforin. Although we did not find other evidence of a distinct localization of perforin and TCR in subcompartments within a common lytic compartment, our data obtained with confocal microscopy, fast deconvolution microscopy, and TIRF microscopy do not rule out this possibility. It is, however, obvious that perforin and CD3-endo do not colocalize.

An important parameter of the immune response is the speed of target cell killing by CTL because it determines the efficiency of cell killing. Using data sets acquired with confocal microscopy (as shown in Fig. 2), we modeled vesicle transport using a compartment model as sketched in Fig. 8A and formulated the dynamic changes in the various vesicle pools mathematically. The rate constants obtained from the model predict the numbers of paired and single LG in different areas of the cell (for instance, in the area in proximity to the IS) over time (solid lines in Fig. 8B). These predictions are in good agreement with the experimental data (squares and circles in Fig. 8B), indicating that the model is appropriate to fit the data. One important prediction from the model is that 5 min after IS formation, the transport rate constants are accelerated and the rate of LG production is increased to 1 granule per minute (Table 1). Furthermore, the number of released vesicles increases to a rate of ~ 1 granule per minute immediately after IS formation. We conclude that CTL need only a few minutes to secrete LG at the IS, supporting an en passant killing process. In line with this prediction, Purbhoo et al. (63) have shown that a mature IS is not required for cytotoxicity. They found that CTL were able to detect a single foreign Ag, and three peptide-MHC complexes were necessary for killing but 10 were needed for full signaling including a sustained Ca^{2+} increase.

In summary, we report that the tethering (or pairing) of LG and CD3-endo is required for the enrichment, docking, and release of LG at the IS, which is needed for CTL-dependent target cell killing. Pairing the CD3-endo with LG stabilizes the LG at the IS and enhances the probability of LG release. The SNARE protein Vti1b is necessary for this close interaction between LG and CD3-endo and thus regulates LG accumulation, docking, and release at the IS during target cell killing.

Acknowledgments

We thank Bettina Strauß, Anja Ludes, Claudia Kilter, Carmen Hässig, Carolin Bick, Reiko Trautmann, Melodie-Jo Wolfs, and Carmen Mangerich for technical help, Peter Lipp for the use of the confocal microscope and the qRT-PCR machine, Roger Tsien for providing the mCherry construct, Alexey Khodjakov for providing the γ -tubulin-GFP construct, and Martina Sester for FACS analysis.

Disclosures

The authors have no financial conflicts of interest.

References

- Russell, J. H., and T. J. Ley. 2002. Lymphocyte-mediated cytotoxicity. *Annu. Rev. Immunol.* 20: 323–370.
- Stinchcombe, J. C., and G. M. Griffiths. 2007. Secretory mechanisms in cell-mediated cytotoxicity. *Annu. Rev. Cell Dev. Biol.* 23: 495–517.
- Liu, D., Y. T. Bryceson, T. Meckel, G. Vasiliver-Shamis, M. L. Dustin, and E. O. Long. 2009. Integrin-dependent organization and bidirectional vesicular traffic at cytotoxic immune synapses. *Immunity* 31: 99–109.
- Griffiths, G. M., A. Tsun, and J. C. Stinchcombe. 2010. The immunological synapse: a focal point for endocytosis and exocytosis. *J. Cell Biol.* 189: 399–406.
- Pores-Fernando, A. T., and A. Zweifach. 2009. Calcium influx and signaling in cytotoxic T-lymphocyte lytic granule exocytosis. *Immunol. Rev.* 231: 160–173.
- Barry, M., and R. C. Bleackley. 2002. Cytotoxic T lymphocytes: all roads lead to death. *Nat. Rev. Immunol.* 2: 401–409.
- Jacobelli, J., P. G. Andres, J. Boisvert, and M. F. Krummel. 2004. New views of the immunological synapse: variations in assembly and function. *Curr. Opin. Immunol.* 16: 345–352.
- Dustin, M. L. 2008. T-cell activation through immunological synapses and kinapses. *Immunol. Rev.* 221: 77–89.
- Krummel, M. F., and I. Macara. 2006. Maintenance and modulation of T cell polarity. *Nat. Immunol.* 7: 1143–1149.
- Liu, H., M. Rhodes, D. L. Wiest, and D. A. Vignali. 2000. On the dynamics of TCR:CD3 complex cell surface expression and downmodulation. *Immunity* 13: 665–675.
- Alcover, A., and B. Alarcón. 2000. Internalization and intracellular fate of TCR-CD3 complexes. *Crit. Rev. Immunol.* 20: 325–346.
- Das, V., B. Nal, A. Dujeancourt, M. I. Thoulouze, T. Galli, P. Roux, A. Dautry-Varsat, and A. Alcover. 2004. Activation-induced polarized recycling targets T cell antigen receptors to the immunological synapse; involvement of SNARE complexes. *Immunity* 20: 577–588.
- Lee, K. H., A. D. Holdorf, M. L. Dustin, A. C. Chan, P. M. Allen, and A. S. Shaw. 2002. T cell receptor signaling precedes immunological synapse formation. *Science* 295: 1539–1542.
- Choudhuri, K., and P. A. van der Merwe. 2007. Molecular mechanisms involved in T cell receptor triggering. *Semin. Immunol.* 19: 255–261.
- Peters, P. J., J. Borst, V. Oorschot, M. Fukuda, O. Krähenbühl, J. Tschopp, J. W. Slot, and H. J. Geuze. 1991. Cytotoxic T lymphocyte granules are secretory lysosomes, containing both perforin and granzymes. *J. Exp. Med.* 173: 1099–1109.
- Peters, P. J., H. J. Geuze, H. A. Van der Donk, J. W. Slot, J. M. Griffith, N. J. Stam, H. C. Clevers, and J. Borst. 1989. Molecules relevant for T cell-target cell interaction are present in cytolytic granules of human T lymphocytes. *Eur. J. Immunol.* 19: 1469–1475.
- Huse, M., E. J. Quann, and M. M. Davis. 2008. Shouts, whispers and the kiss of death: directional secretion in T cells. *Nat. Immunol.* 9: 1105–1111.
- Lyubchenko, T. A., G. A. Wurth, and A. Zweifach. 2001. Role of calcium influx in cytotoxic T lymphocyte lytic granule exocytosis during target cell killing. *Immunity* 15: 847–859.
- Orange, J. S., K. E. Harris, M. M. Andzelm, M. M. Valter, R. S. Geha, and J. L. Strominger. 2003. The mature activating natural killer cell immunologic synapse is formed in distinct stages. *Proc. Natl. Acad. Sci. USA* 100: 14151–14156.
- Katz, P., A. M. Zaytoun, and J. H. Lee Jr. 1982. Mechanisms of human cell-mediated cytotoxicity. III. Dependence of natural killing on microtubule and microfilament integrity. *J. Immunol.* 129: 2816–2825.
- Mentlik, A. N., K. B. Sanborn, E. L. Holzbaur, and J. S. Orange. 2010. Rapid lytic granule convergence to the MTOC in natural killer cells is dependent on dynein but not cytotytic commitment. *Mol. Biol. Cell* 21: 2241–2256.
- Sanborn, K. B., G. D. Rak, S. Y. Maru, K. Demers, A. Difeo, J. A. Martignetti, M. R. Betts, R. Favier, P. P. Banerjee, and J. S. Orange. 2009. Myosin IIA associates with NK cell lytic granules to enable their interaction with F-actin and function at the immunological synapse. *J. Immunol.* 182: 6969–6984.
- Stinchcombe, J. C., E. Majorovits, G. Bossi, S. Fuller, and G. M. Griffiths. 2006. Centrosome polarization delivers secretory granules to the immunological synapse. *Nature* 443: 462–465.
- Jenkins, M. R., and G. M. Griffiths. 2010. The synapse and cytolytic machinery of cytotoxic T cells. *Curr. Opin. Immunol.* 22: 1–6.
- Jenkins, M. R., A. Tsun, J. C. Stinchcombe, and G. M. Griffiths. 2009. The strength of T cell receptor signal controls the polarization of cytotoxic machinery to the immunological synapse. *Immunity* 31: 621–631.
- Beal, A. M., N. Anikeeva, R. Varma, T. O. Cameron, G. Vasiliver-Shamis, P. J. Norris, M. L. Dustin, and Y. Sykulev. 2009. Kinetics of early T cell receptor signaling regulate the pathway of lytic granule delivery to the secretory domain. *Immunity* 31: 632–642.
- Zur Stadt, U., K. Beutel, S. Kolberg, R. Schneppenheim, H. Kabisch, G. Janka, and H. C. Hennies. 2006. Mutation spectrum in children with primary hemophagocytic lymphohistiocytosis: molecular and functional analyses of PRF1, UNC13D, STX11, and RAB27A. *Hum. Mutat.* 27: 62–68.
- Stow, J. L., A. P. Manderson, and R. Z. Murray. 2006. SNAREing immunity: the role of SNAREs in the immune system. *Nat. Rev. Immunol.* 6: 919–929.
- Stinchcombe, J., G. Bossi, and G. M. Griffiths. 2004. Linking albinism and immunity: the secrets of secretory lysosomes. *Science* 305: 55–59.
- Feldmann, J., I. Callebaut, G. Raposo, S. Certain, D. Bacq, C. Dumont, N. Lambert, M. Ouachée-Chardin, G. Chedeville, H. Tamary, et al. 2003. Munc13-4 is essential for cytolytic granules fusion and is mutated in a form of familial hemophagocytic lymphohistiocytosis (FHL3). *Cell* 115: 461–473.
- zur Stadt, U., S. Schmidt, B. Kasper, K. Beutel, A. S. Diler, J. I. Henter, H. Kabisch, R. Schneppenheim, P. Nürnberg, G. Janka, and H. C. Hennies. 2005. Linkage of familial hemophagocytic lymphohistiocytosis (FHL) type-4 to chromosome 6q24 and identification of mutations in syntaxin 11. *Hum. Mol. Genet.* 14: 827–834.
- zur Stadt, U., J. Rohr, W. Seifert, F. Koch, S. Grieve, J. Pagel, J. Strauss, B. Kasper, G. Nürnberg, C. Becker, et al. 2009. Familial hemophagocytic lymphohistiocytosis type 5 (FHL-5) is caused by mutations in Munc18-2 and impaired binding to syntaxin 11. *Am. J. Hum. Genet.* 85: 482–492.
- Dressel, R., L. Elsner, P. Novota, N. Kanwar, and G. Fischer von Mollard. 2010. The exocytosis of lytic granules is impaired in Vti1b- or Vamp8-deficient CTL leading to a reduced cytotoxic activity following antigen-specific activation. *J. Immunol.* 185: 1005–1014.

34. Südhof, T. C., and J. E. Rothman. 2009. Membrane fusion: grappling with SNARE and SM proteins. *Science* 323: 474–477.
35. Becherer, U., and J. Rettig. 2006. Vesicle pools, docking, priming, and release. *Cell Tissue Res.* 326: 393–407.
36. Jahn, R., and R. H. Scheller. 2006. SNAREs—engines for membrane fusion. *Nat. Rev. Mol. Cell Biol.* 7: 631–643.
37. Huse, M., B. F. Lillemeier, M. S. Kuhns, D. S. Chen, and M. M. Davis. 2006. T cells use two directionally distinct pathways for cytokine secretion. *Nat. Immunol.* 7: 247–255.
38. Pattu, V., B. Qu, M. Marshall, U. Becherer, C. Junker, U. Matti, E. C. Schwarz, E. Krause, M. Hoth, and J. Rettig. 2011. Syntaxin7 is required for lytic granule release from cytotoxic T lymphocytes. *Traffic*. DOI: 10.1111/j.1600-0854.2011.01193.x.
39. Schwarz, E. C., C. Kummerow, A. S. Wenning, K. Wagner, A. Sappok, K. Waggershauer, D. Griesemer, B. Strauss, M. J. Wolfs, A. Quintana, and M. Hoth. 2007. Calcium dependence of T cell proliferation following focal stimulation. *Eur. J. Immunol.* 37: 2723–2733.
40. Lang, K. S., A. Moris, C. Gouttefangeas, S. Walter, V. Teichgräber, M. Miller, D. Wernet, K. Hamprecht, H. G. Rammensee, and S. Stevanovic. 2002. High frequency of human cytomegalovirus (HCMV)-specific CD8+ T cells detected in a healthy CMV-seropositive donor. *Cell. Mol. Life Sci.* 59: 1076–1080.
41. Wagner, C., F. Neumann, B. Kubuschok, E. Regitz, A. Mischo, S. Stevanovic, M. Friedrich, W. Schmidt, H. G. Rammensee, and M. Pfreundschuh. 2003. Identification of an HLA-A*02 restricted immunogenic peptide derived from the cancer testis antigen HOM-MEL-40/SSX2. *Cancer Immun.* 3: 18.
42. zum Büschenfelde, C. M., J. Metzger, C. Hermann, N. Nicklisch, C. Peschel, and H. Bernhard. 2001. The generation of both T killer and Th cell clones specific for the tumor-associated antigen HER2 using retrovirally transduced dendritic cells. *J. Immunol.* 167: 1712–1719.
43. Quintana, A., C. Schwindling, A. S. Wenning, U. Becherer, J. Rettig, E. C. Schwarz, and M. Hoth. 2007. T cell activation requires mitochondrial translocation to the immunological synapse. *Proc. Natl. Acad. Sci. USA* 104: 14418–14423.
44. Mantei, A., S. Rutz, M. Janke, D. Kirchhoff, U. Jung, V. Patzel, U. Vogel, T. Rudel, I. Andreou, M. Weber, and A. Scheffold. 2008. siRNA stabilization prolongs gene knockdown in primary T lymphocytes. *Eur. J. Immunol.* 38: 2616–2625.
45. Rozen, S., and H. Skaletsky. 2000. Primer3 on the WWW for general users and for biologist programmers. *Methods Mol. Biol.* 132: 365–386.
46. Press, W. H., S. A. Teukolsky, W. T. Vetterling, and B. P. Flannery. 1988. *Numerical Recipes*. Cambridge University Press Cambridge, MA, p. 274–328.
47. Kupfer, A., S. L. Swain, and S. J. Singer. 1987. The specific direct interaction of helper T cells and antigen-presenting B cells. II. Reorientation of the microtubule organizing center and reorganization of the membrane-associated cytoskeleton inside the bound helper T cells. *J. Exp. Med.* 165: 1565–1580.
48. Martín-Cófreces, N. B., J. Robles-Valero, J. R. Cabrero, M. Mittelbrunn, M. Gordón-Alonso, C. H. Sung, B. Alarcón, J. Vázquez, and F. Sánchez-Madrid. 2008. MTOC translocation modulates IS formation and controls sustained T cell signaling. *J. Cell Biol.* 182: 951–962.
49. Sheff, D., L. Pelletier, C. B. O'Connell, G. Warren, and I. Mellman. 2002. Transferrin receptor recycling in the absence of perinuclear recycling endosomes. *J. Cell Biol.* 156: 797–804.
50. van Dam, E. M., T. Ten Broeke, K. Jansen, P. Spijkers, and W. Stoorvogel. 2002. Endocytosed transferrin receptors recycle via distinct dynamin and phosphatidylinositol 3-kinase-dependent pathways. *J. Biol. Chem.* 277: 48876–48883.
51. Vonderheit, A., and A. Helenius. 2005. Rab7 associates with early endosomes to mediate sorting and transport of Semliki forest virus to late endosomes. *PLoS Biol.* 3: e233.
52. Betts, M. R., J. M. Brechley, D. A. Price, S. C. De Rosa, D. C. Douek, M. Roederer, and R. A. Koup. 2003. Sensitive and viable identification of antigen-specific CD8+ T cells by a flow cytometric assay for degranulation. *J. Immunol. Methods* 281: 65–78.
53. Rubio, V., T. B. Stuge, N. Singh, M. R. Betts, J. S. Weber, M. Roederer, and P. P. Lee. 2003. Ex vivo identification, isolation and analysis of tumor-cytolytic T cells. *Nat. Med.* 9: 1377–1382.
54. Offenhauser, C., N. Lei, S. Roy, B. M. Collins, J. L. Stow, and R. Z. Murray. 2011. Syntaxin 11 binds Vti1b and regulates late endosome to lysosome fusion in macrophages. *Traffic* March 9. doi:10.1111/j.1600-0854.2011.01189.x
55. Zweifach, A. 2000. Target-cell contact activates a highly selective capacitative calcium entry pathway in cytotoxic T lymphocytes. *J. Cell Biol.* 148: 603–614.
56. Wiedemann, A., D. Depoil, M. Faroudi, and S. Valitutti. 2006. Cytotoxic T lymphocytes kill multiple targets simultaneously via spatiotemporal uncoupling of lytic and stimulatory synapses. *Proc. Natl. Acad. Sci. USA* 103: 10985–10990.
57. Purdie, B., L. A. Pitcher, N. S. van Oers, and C. Wülfing. 2005. T cell receptor (TCR) clustering in the immunological synapse integrates TCR and costimulatory signaling in selected T cells. *Proc. Natl. Acad. Sci. USA* 102: 2904–2909.
58. de Brito, O. M., and L. Scorrano. 2008. Mitofusin 2 tethers endoplasmic reticulum to mitochondria. *Nature* 456: 605–610.
59. Manderson, A. P., J. G. Kay, L. A. Hammond, D. L. Brown, and J. L. Stow. 2007. Subcompartments of the macrophage recycling endosome direct the differential secretion of IL-6 and TNFalpha. *J. Cell Biol.* 178: 57–69.
60. Weisswange, I., T. P. Newsome, S. Schleich, and M. Way. 2009. The rate of N-WASP exchange limits the extent of ARP2/3-complex-dependent actin-based motility. *Nature* 458: 87–91.
61. Bright, N. A., B. J. Reaves, B. M. Mullock, and J. P. Luzio. 1997. Dense core lysosomes can fuse with late endosomes and are re-formed from the resultant hybrid organelles. *J. Cell Sci.* 110: 2027–2040.
62. Ménager, M. M., G. Ménasché, M. Romao, P. Knapnougel, C. H. Ho, M. Garfa, G. Raposo, J. Feldmann, A. Fischer, and G. de Saint Basile. 2007. Secretory cytotoxic granule maturation and exocytosis require the effector protein hMunc13-4. *Nat. Immunol.* 8: 257–267.
63. Purbhoo, M. A., D. J. Irvine, J. B. Huppa, and M. M. Davis. 2004. T cell killing does not require the formation of a stable mature immunological synapse. *Nat. Immunol.* 5: 524–530.